



Facile Fabrication of Fe₃O₄@TiO₂@C Yolk–Shell Spheres as Anode Material for Lithium Ion Batteries

Wenming Liao^{1,2} · Zhongqiang Shan¹ · Jianhua Tian¹

Received: 28 August 2019 / Revised: 10 October 2019 / Accepted: 4 November 2019 / Published online: 9 December 2019
© Tianjin University and Springer-Verlag GmbH Germany, part of Springer Nature 2019

Abstract

Transition metal oxides have been actively exploited for application in lithium ion batteries due to their facile synthesis, high specific capacity, and environmental-friendly. In this paper, Fe₃O₄@TiO₂@C yolk–shell (Y–S) spheres, used as anode material for lithium ion batteries, were successfully fabricated by Stöber method. XRD patterns reveal that Fe₃O₄@TiO₂@C Y–S spheres possess a good crystallinity. But the diffraction peaks' intensity of Fe₃O₄ crystals in the composites is much weaker than that of bare Fe₃O₄ spheres, indicating that the outer anatase TiO₂@C layer can cover up the diffraction peaks of inner Fe₃O₄ spheres. The yolk–shell structure of Fe₃O₄@TiO₂@C spheres is further characterized by TEM, HAADF-STEM, and EDS mapping. The yolk–shell structure is good for improving the cycling stability of the inner Fe₃O₄ spheres during lithium ions insertion–extraction processes. When tested at 200 mA/g, the Fe₃O₄@TiO₂@C Y–S spheres can provide a stable discharge capacity of 450 mAh/g over 100 cycles, which is much better than that of bare Fe₃O₄ spheres and TiO₂@C spheres. Furthermore, cyclic voltammetry curves show that the composites have a good cycling stability compared to bare Fe₃O₄ spheres.

Keywords Fe₃O₄@TiO₂@C yolk–shell spheres · Cycle performance · Lithium ion batteries · Anode material

Introduction

Rechargeable lithium ion batteries (LIBs) have been regarded as the most popular electrochemical energy storage devices used in hybrid electrical vehicles, electrical vehicles, and handheld electronic equipment [1–3]. Lots of transition metal oxides, such as SnO₂ [4, 5], Co₃O₄ [6, 7], MnO₂ [8, 9], NiO [10, 11], and Fe₃O₄ [12, 13], have been used as anodes in LIBs to date. Iron oxides, as an alternative of graphite, have been recognized as promising candidates due to their high specific capacities (above 1000 mAh/g), abundant resources, environmental benignity, and low cost. However, the serious volume expansion of magnetic iron oxides during the lithiation–delithiation processes is a fatal defect for application in LIBs. A series of associated problems such as the cracking of active materials, the collapse of

electrode structure, and electrode polarization [14–18] result in an extremely bad cycle stability and rate performance. Resolving such problems would thus be beneficial.

Nowadays, coating a layer of stable electrochemical materials is considered to be effective for stabilizing the electrochemical properties of iron oxides in the lithium ions insertion–extraction processes, such as Fe₃O₄@porous carbon [14], Fe₃O₄/carbon composites [15], mesoporous Fe₃O₄@C submicrospheres [16], and porous Fe₃O₄@C hollow spheres [19]. Zhang et al. [20] enhanced the cycling performance by coating a layer of TiO₂ to form Fe₂O₃@TiO₂ core–shell (C–S) nanorods, and the results showed high and stable delivered capacities of approximately 860 mAh/g at a high current density of 1000 mA/g. Porous TiO₂ was chosen as the shell, which benefits electrolyte infiltration, restricts excessive volume changes, and prevents collapse and dissolution into the electrolyte of Fe₂O₃ during the discharge–charge processes [20]. The design of yolk–shell (Y–S) structure has also proved to be effective for improving the cycling stability of iron oxides [21]. For example, to increase the conductivity of materials, a unique architecture with Y–S Fe₂O₃@C composites was synthesized by the classic Stöber method, which can prevent the reunion of

✉ Jianhua Tian
jhtian@tju.edu.cn

¹ School of Chemical Engineering and Technology, Tianjin University, Tianjin 300072, China

² School of Chemistry and Chemical Engineering, Jiangangshan University, Jiangxi 343009, China

active materials and support an interior space to alleviate the volume expansion and rupture during discharge–charge experiments. The materials could be found to possess a good cycling stability and provide an excellent rate performance [21]. To relieve the capacity fading of bare metal oxides, other metal oxides with Y–S structures, such as $\text{Cr}_2\text{O}_3@ \text{TiO}_2$ Y–S octahedrons [22], $\text{SnO}_2@ \text{C}$ Y–S nanospheres [23], MnO_x/C Y–S nanorods [24], and $\text{Co}_3\text{O}_4@ \text{TiO}_2@ \text{C}$ Y–S spheres [25], have also been synthesized using a variety of methods to achieve the good electrochemical properties.

In this work, we reported a simple method to synthesize $\text{Fe}_3\text{O}_4@ \text{TiO}_2@ \text{C}$ Y–S spheres for alleviating the capacity attenuation of bare Fe_3O_4 spheres as anodes in LIBs. The materials were physically characterized to investigate the structure, synthesis process, crystal structure, components, and element valence. When tested as anodes of LIBs, the $\text{Fe}_3\text{O}_4@ \text{TiO}_2@ \text{C}$ Y–S spheres show the excellent cycling stability and good rate performance. At 200 mA/g, the reversible capacity of approximately 450 mAh/g is much higher than that of bare Fe_3O_4 spheres (160.2 mAh/g) after 100 cycles. Therefore, constructing Y–S structures is an acceptable strategy to promote the electrochemical performance of transition metal oxides when applied in LIBs.

Experimental

Synthesis of $\text{Fe}_3\text{O}_4@ \text{TiO}_2@ \text{C}$ Y–S Spheres

Fe_3O_4 spheres were synthesized using a method reported in Ref. [12]. First, 0.64 g of sodium dodecyl benzene sulfonate was added to 60 mL of ethylene glycol to form a clear solution, and 2.16 g of $\text{FeCl}_3 \cdot 6\text{H}_2\text{O}$ and 3.72 g of sodium acetate were then mixed in the above solution under vigorous stirring for several hours. The obtained solution was transferred into a 100-mL Teflon-lined autoclave, and the oven temperature was increased to 190 °C for 15 h. Finally, a brown product was collected by centrifugation and washed with ethanol/water five times.

The synthesis method of $\text{Fe}_3\text{O}_4@ \text{SiO}_2@ \text{TiO}_2$ C–S spheres was similar to that reported in Ref. [26]. The as-synthesized Fe_3O_4 spheres were dispersed in a mixed solution of 150 mL ethanol/water ($V/V=4:1$) using ultrasonication and vigorous agitation. 1 mL of ammonia and 1 mL of tetraethylorthosilane (TEOS) were successively and slowly added to the above solution to form $\text{Fe}_3\text{O}_4@ \text{SiO}_2$ C–S spheres. 0.1 g of $\text{Fe}_3\text{O}_4@ \text{SiO}_2$ C–S spheres was then dispersed in an ethanol (120 mL)/water (0.5 mL) solution containing hydroxypropyl cellulose (HPC) by repeated ultrasonication and continuous vigorous stirring for 10 h. Finally, tetra-*n*-butyl titanate (TBOT, 0.6 mL) ethanol solution was slowly added into the above mixed solution to form $\text{Fe}_3\text{O}_4@ \text{SiO}_2@ \text{TiO}_2$ C–S spheres.

Through hydrothermal carbonization treatment, a layer of carbon was coated to improve the conductivity of the as-prepared samples. First, the $\text{Fe}_3\text{O}_4@ \text{SiO}_2@ \text{TiO}_2$ C–S spheres were dispersed in 60 mL of glucose (300 mg) aqueous solution under ultrasonication. Second, the mixture was transferred into a 100-mL Teflon-lined autoclave and then heated at 180 °C for 6 h in an oven to obtain the $\text{Fe}_3\text{O}_4@ \text{SiO}_2@ \text{TiO}_2@ \text{C}$ C–S spheres. Third, the sample was subsequently annealed at 500 °C for 4 h to further carbonize in an argon atmosphere at a heating rate of 2 °C/min. Finally, the sacrificial SiO_2 layer was removed by immersing in 60 mL of LiOH aqueous solution (0.06 mol/L) to obtain the final product ($\text{Fe}_3\text{O}_4@ \text{TiO}_2@ \text{C}$ Y–S spheres) at 90 °C.

Material Characterization

Scanning electron microscopy (SEM, S4800, HITACHI, Japan) and transmission electron microscopy (TEM, Tecnai G2 F20, FEI Company, USA) were employed to observe the morphologies and sizes of samples. Energy-dispersive X-ray spectrometer (EDS, HITACHI, Japan) was used to further investigate the elements and their distribution in the materials. X-ray powder diffractometer (XRD, Bruker AXS, D8-Focus) was employed to determine the crystal structure of samples by using $\text{Cu-K}\alpha$ irradiation in a range of 10° to 80°. The Raman spectra (DXR Microscope, Thermo Electron Corporation, USA) were collected using Raman microscope to characterize the carbon atom and crystal structure of $\text{Fe}_3\text{O}_4@ \text{TiO}_2@ \text{C}$ Y–S spheres.

Electrochemical Measurements

CR2032 coin-type cells were assembled in an Ar-filled glove box to measure the electrochemical properties of samples. The working electrodes were composed of active materials, acetylene black, and polyvinylidene fluoride at a mass ratio of 7:2:1. The loading mass weight density of active materials is approximately 1.0–1.1 mg/cm². 1.0 mol/L LiPF_6 in a mixed solvent of ethylene carbonate and diethyl carbonate (DEC) ($V/V=1:1$) served as the electrolyte, and circular metal Li foils were used as counter electrodes in the CR2032 coin-type cells. The discharge–charge measurements of cells were conducted on a Land battery test system in a potential range of 3.0 V to 0.01 V versus Li/Li^+ . Cyclic voltammetry (CV) tests were conducted on a CHI660D electrochemical workstation at different scan rates of 0.10 mV/s and 0.50 mV/s between 3.0 and 0.01 V.

Results and Discussion

Figure 1a shows a schematic diagram of the stepwise synthesis of $\text{Fe}_3\text{O}_4@ \text{TiO}_2@ \text{C}$ Y–S spheres, as described in the experimental section. First, Fe_3O_4 spheres with various sizes were synthesized using a simple hydrothermal method. SEM image shows that the diameters of large Fe_3O_4 spheres are about 200–300 nm, while those of smaller Fe_3O_4 spheres are only dozens of nanometers (Fig. 1b). Second, a thin SiO_2 layer was coated on the surface of Fe_3O_4 spheres to form $\text{Fe}_3\text{O}_4@ \text{SiO}_2$ C–S spheres with a very smooth surface by the hydrolysis of TEOS in an alkaline aqueous solution (Fig. 1c). Third, the outer TiO_2 shell was coated on the surface of the SiO_2 layer to obtain $\text{Fe}_3\text{O}_4@ \text{SiO}_2@ \text{TiO}_2$ C–S spheres by the hydrolysis of TBOT. SEM image shows that the obtained material became much coarser (Fig. 1d). Fourth, the $\text{Fe}_3\text{O}_4@ \text{SiO}_2@ \text{TiO}_2@ \text{C}$ C–S spheres were formed by the hydrolysis of glucose, followed by calcination at 500 °C. Finally, the middle SiO_2 layer as sacrificial template was removed by immersing in a LiOH aqueous solution and the $\text{Fe}_3\text{O}_4@$

$\text{TiO}_2@ \text{C}$ Y–S spheres were obtained. Figure 1e shows that the final product has an uneven size distribution ranging from dozens of nanometers to 800 nm. It is also of note that many spheres ($\text{Fe}_3\text{O}_4@ \text{SiO}_2$, $\text{Fe}_3\text{O}_4@ \text{SiO}_2@ \text{TiO}_2$, and $\text{Fe}_3\text{O}_4@ \text{TiO}_2@ \text{C}$ spheres) were reunited after coating SiO_2 and TiO_2 layers.

The sizes, morphologies, and internal structures of samples were characterized using TEM. As evident from the TEM images shown in Fig. 2a, the Fe_3O_4 spheres have a size distribution ranging from several nanometers to 300 nm. After hydrolysis of TEOS, the SiO_2 shell with a thickness of 20–30 nm was coated on the surface of Fe_3O_4 spheres to form $\text{Fe}_3\text{O}_4@ \text{SiO}_2$ C–S spheres. Meanwhile, a lot of small SiO_2 spheres were synthesized in this process (Fig. 2b). After coating the $\text{TiO}_2@ \text{C}$ shell and then removing the SiO_2 layer, it can be found from TEM images (Fig. 2c, d) that $\text{Fe}_3\text{O}_4@ \text{TiO}_2@ \text{C}$ Y–S spheres have a very unambiguous internal void space, and the width between the Fe_3O_4 sphere and TiO_2 shell is about 20 nm. Notably, a large number of smaller spheres with sizes ranging from dozens to hundreds of nanometers exist in the final product. It can be attributed to three reasons: (1) Small $\text{Fe}_3\text{O}_4@ \text{TiO}_2@ \text{C}$ Y–S spheres

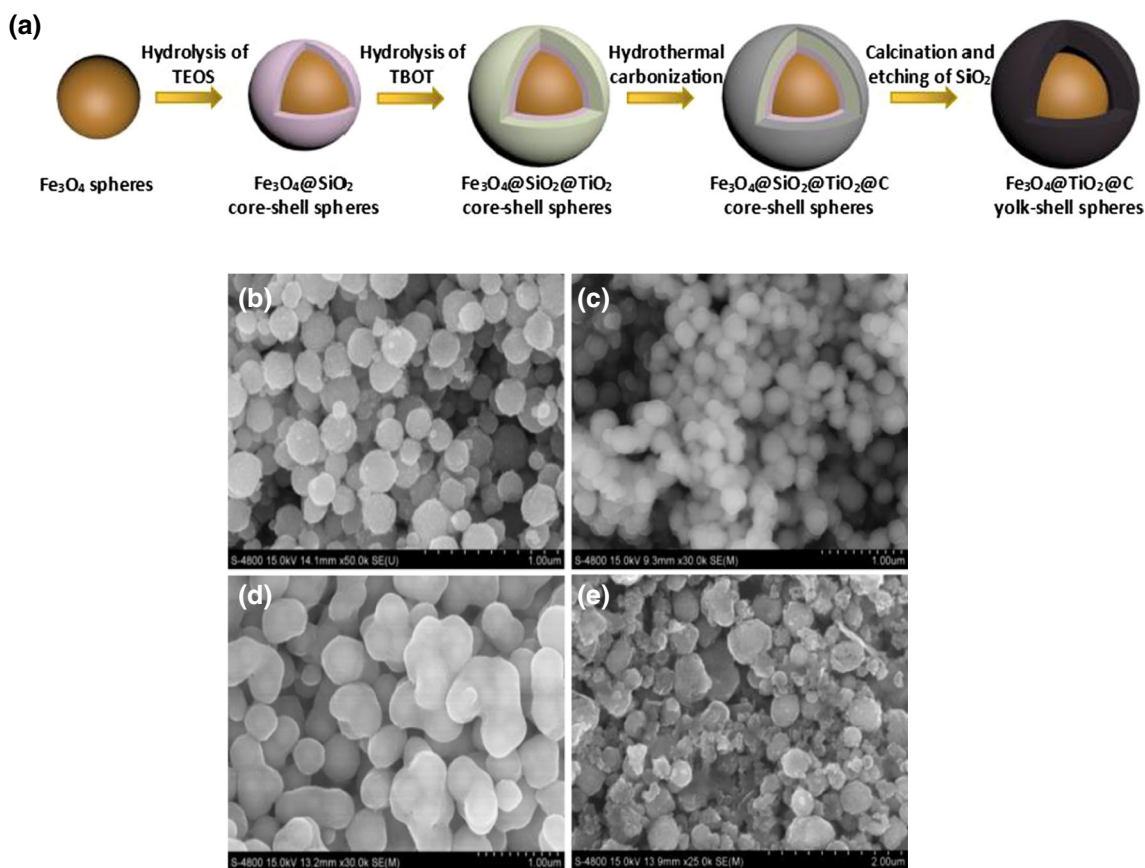
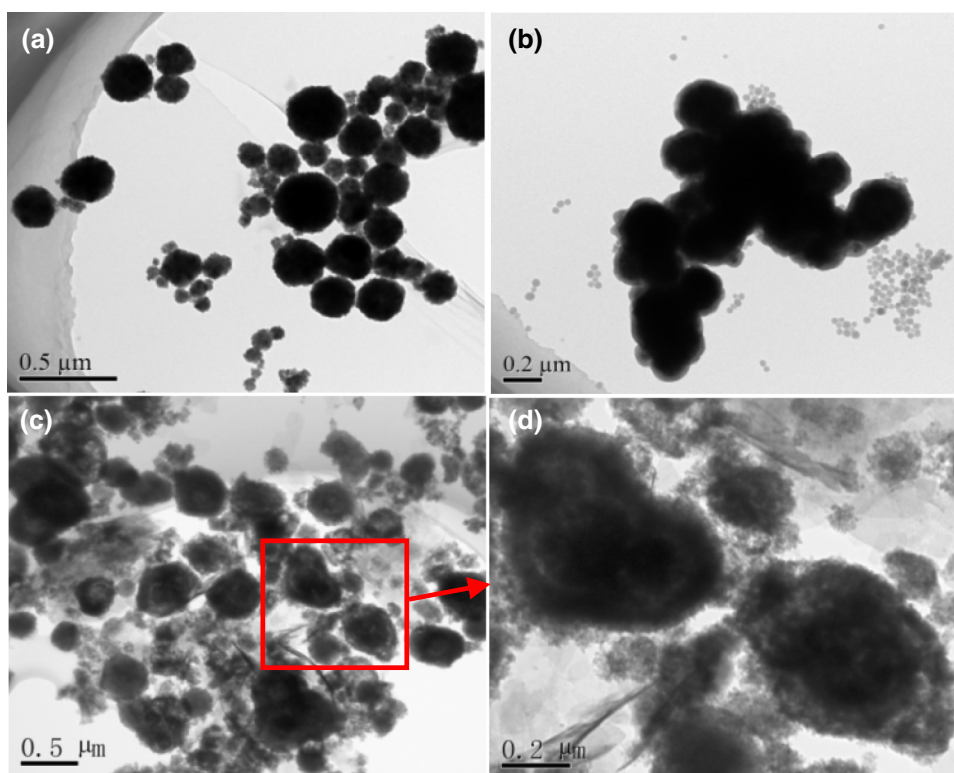


Fig. 1 a Schematic diagram showing stepwise synthesis of $\text{Fe}_3\text{O}_4@ \text{TiO}_2@ \text{C}$ Y–S spheres. SEM images of **b** Fe_3O_4 spheres, **c** $\text{Fe}_3\text{O}_4@ \text{SiO}_2$ C–S spheres, **d** $\text{Fe}_3\text{O}_4@ \text{SiO}_2@ \text{TiO}_2$ C–S spheres, and **e** $\text{Fe}_3\text{O}_4@ \text{TiO}_2@ \text{C}$ Y–S spheres

Fig. 2 TEM images of **a** Fe_3O_4 spheres, **b** $\text{Fe}_3\text{O}_4@ \text{SiO}_2$ C-S spheres, and **c** $\text{Fe}_3\text{O}_4@ \text{TiO}_2@ \text{C}$ Y-S spheres. **d** Local magnification TEM image of $\text{Fe}_3\text{O}_4@ \text{TiO}_2@ \text{C}$ Y-S spheres



and $\text{TiO}_2@ \text{C}$ hollow spheres were synthesized using small $\text{Fe}_3\text{O}_4@ \text{SiO}_2$ C-S spheres and SiO_2 spheres as templates, respectively; (2) the aggregation of TiO_2 nanoparticles occurred in the hydrolysis process of TBOT; and (3) the collapse of outer layer TiO_2 shells resulted in the formation of smaller TiO_2 nanocrystals in the alkaline thermal etching process.

EDS analysis and elemental mapping were applied to determine the components, elements, and their distribution in $\text{Fe}_3\text{O}_4@ \text{TiO}_2@ \text{C}$ Y-S spheres. EDS analysis clearly shows that the composites contain the elements of titanium, oxide, iron, and silicon (Fig. 3a), and the silicon content is very low. Calculation of the elemental contents (Table 1) shows that the mass ratio of Fe_3O_4 to TiO_2 is 2.33:10. The

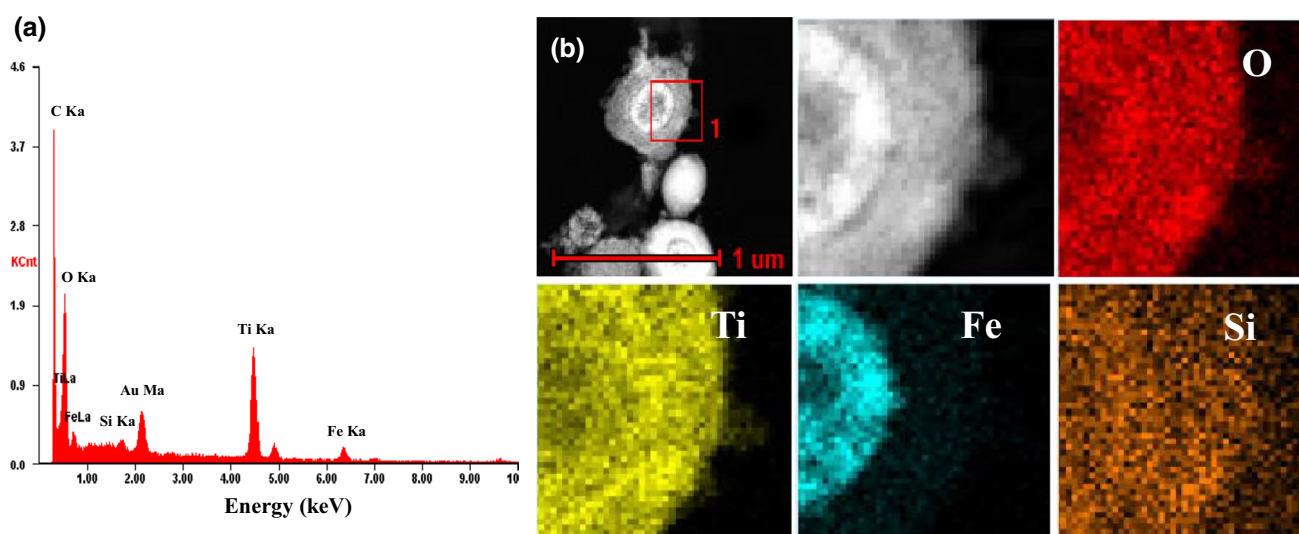


Fig. 3 **a** EDS analysis image of $\text{Fe}_3\text{O}_4@ \text{TiO}_2@ \text{C}$ Y-S spheres; **b** HAADF image and EDS elemental mapping images of oxygen, titanium, iron, and silicon in the $\text{Fe}_3\text{O}_4@ \text{TiO}_2@ \text{C}$ Y-S spheres

Table 1 EDS analysis result of Fe₃O₄@TiO₂@C Y–S spheres

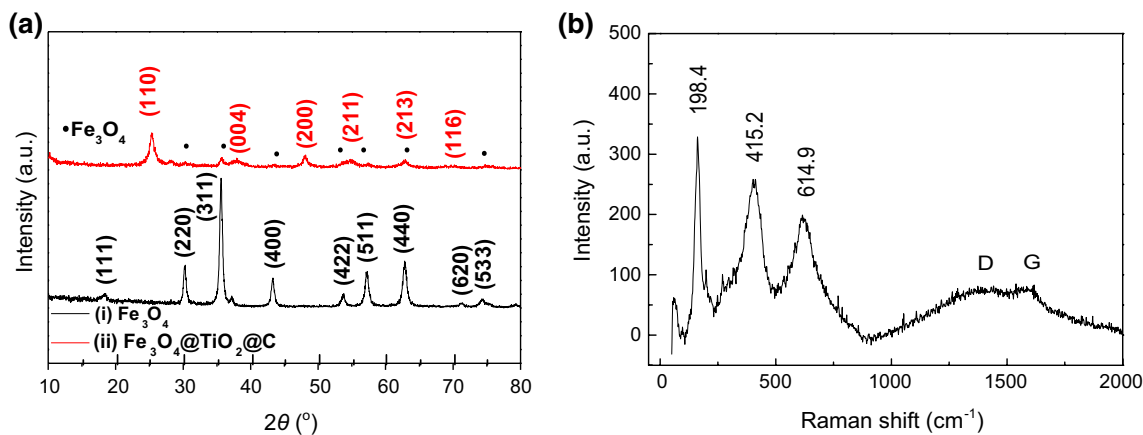
Element	Mass ratio (%)	Atomic ratio (%)
C	35.24	53.98
O	31.64	36.38
Si	0.53	0.35
Ti	17.49	6.72
Fe	4.90	1.62
Au	10.19	0.95

high angle annular dark field (HAADF) image shows the existence of an unambiguous void space/boundary layer between Fe₃O₄ sphere and TiO₂@C shell. Figure 3b shows that oxygen element is distributed in the entire sphere, while iron element is only distributed in the center of the material, which further proves that the Fe₃O₄ sphere is located inside Fe₃O₄@TiO₂@C Y–S sphere. In contrast, silicon element is discretely dispersed in the Fe₃O₄@TiO₂@C Y–S sphere, and this behavior is obviously different from that of other elements and is mainly ascribed to the absorption of only a small amount of SiO₂ on the surface of Fe₃O₄@TiO₂@C Y–S spheres during the alkaline thermal etching process.

The X-ray powder diffraction (XRD) patterns of Fe₃O₄ spheres and Fe₃O₄@TiO₂@C Y–S spheres are shown in Fig. 4a, and curve (i) shows that the diffraction peaks of 2θ at 18.5°, 30.3°, 35.6°, 43.3°, 53.8°, 57.3°, 62.8°, 71.4°, and 74.4° are indexed to the planes (111), (220), (311), (400), (422), (511), (440), (620), and (533) of magnetic cubic phase Fe₃O₄ crystals (JCPDS No. 19-0629), respectively. When the Fe₃O₄ spheres were parceled by TiO₂@C to form Fe₃O₄@TiO₂@C Y–S spheres, the diffraction peaks (marked by the symbol ·) of Fe₃O₄ crystals become much weaker, as shown in curve (ii) of Fig. 4a. The 2θ at 25.36°, 37.96°, 48.16°, 55.02°, 62.26°, and 68.8° corresponds to the planes (110), (004), (200), (211), (213) and (116) of anatase TiO₂ crystals.

The higher crystallinity of Fe₃O₄@TiO₂@C Y–S spheres can be ascribed to the lower carbon content and the lower alkali thermal temperature, and this is evidently different from that of Co₃O₄@TiO₂@C Y–S spheres in Ref. [25]. The Raman spectrum of Fe₃O₄@TiO₂@C Y–S spheres is shown in Fig. 4b. The peaks at 198.4 cm⁻¹ and 614.9 cm⁻¹ are derived from the anatase TiO₂ crystals [27], and the peak at 415.2 cm⁻¹ is ascribed to iron oxides [28]. Furthermore, the elemental carbon of Fe₃O₄@TiO₂@C Y–S spheres is confirmed from the D-band (1320 cm⁻¹) and G-band (1620 cm⁻¹) [29, 30].

The galvanostatic cycling performances and coulombic efficiencies curves of Fe₃O₄@TiO₂@C Y–S spheres, Fe₃O₄ spheres, and TiO₂@C hollow spheres at 200 mA/g are presented in Fig. 5. The first discharge capacity of Fe₃O₄@TiO₂@C Y–S spheres is 778.1 mAh/g with a very low coulombic efficiency of 48.2%. Such a large irreversible capacity loss is mainly derived from the irreversible decomposition of electrolyte, the solid electrolyte interface (SEI) films formed in the electrode, and the trapping of lithium ions inside TiO₂ and Fe₃O₄ lattices [12, 14–17, 19, 20]. The second discharge capacity is reduced to only 523.6 mAh/g, and the subsequently delivered capacities show a slightly declining trend. To the 18th cycle, the discharge capacity reaches the lowest value of 402.8 mAh/g and then rises slowly to around 450 mAh/g over 100 cycles. This occurs because electrolyte infiltration gradually increases in the porous materials to improve the electron transfer and Li-ion migration rate with the number of cycles [31]. The coulombic efficiencies are nearly 100% after five cycles, which indicates that a layer of stable SEI films has formed on the surface of the electrode, and the Fe₃O₄@TiO₂@C Y–S spheres have a good electrochemical Li-inserted reversibility. In contrast, the bare Fe₃O₄ spheres have poor electrochemical properties (Fig. 5a). The first discharge capacity reaches 1082 mAh/g with a high coulombic efficiency of 70.7% (Fig. 5b), but the

**Fig. 4** **a** XRD patterns of Fe₃O₄ spheres and Fe₃O₄@TiO₂@C Y–S spheres; **b** Raman spectrum of Fe₃O₄@TiO₂@C Y–S spheres

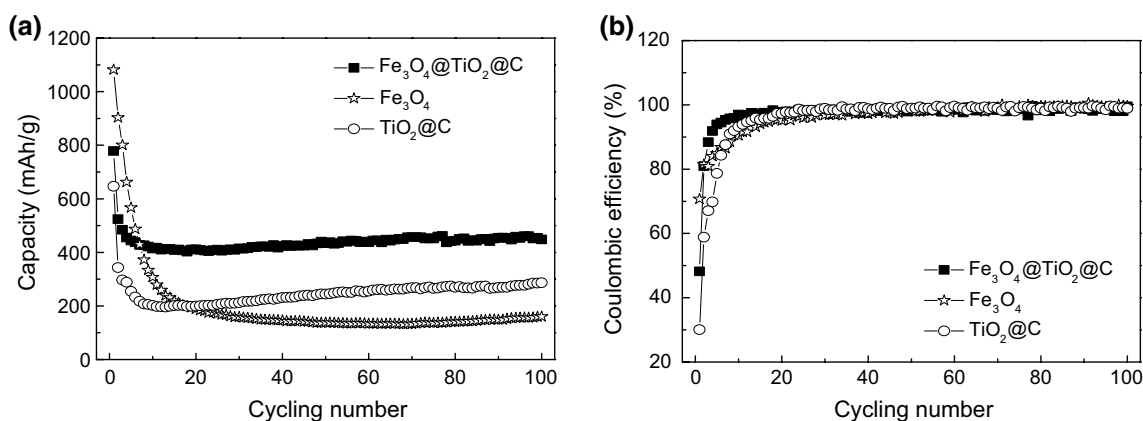


Fig. 5 **a** Galvanostatic cycling tests and **b** coulombic efficiencies of Fe₃O₄@TiO₂@C Y-S spheres, Fe₃O₄ spheres, and TiO₂@C hollow spheres at a current density of 200 mA/g

delivered capacities of the bare Fe₃O₄ spheres decay very quickly. After 10 cycles and 100 cycles, the discharge capacities drop to 307.1 mAh/g and 160.2 mAh/g, respectively, which are far lower than those of the composites under the same test conditions. As such, the high and stable reversible capacities of Fe₃O₄@TiO₂@C Y-S spheres are attributed to two aspects: First, the internal void space formed by the removal of SiO₂ effectively alleviates the volumetric variation in Fe₃O₄ spheres, and second, the TiO₂@C shell effectively restrains the pulverized inner Fe₃O₄ spheres to relieve the electrode polarization and capacity fading, thus leading to an obvious improvement in cycling stability [14, 16, 19–21]. The first discharge capacity of TiO₂@C hollow spheres is 646.5 mAh/g with a very low coulombic efficiency of 30.1%, but the second discharge capacity is only 343.0 mAh/g (Fig. 5). After 100 cycles, the discharge capacity is maintained at 286.5 mAh/g. The delivered capacities of TiO₂@C hollow spheres are obviously much lower than those of Fe₃O₄@TiO₂@C Y-S spheres over 100 cycles. These obtained data clearly show that the capacities of Fe₃O₄@TiO₂@C Y-S spheres are largely related to those of the inner Fe₃O₄ spheres. In addition, the first coulombic efficiency of Fe₃O₄@TiO₂@C Y-S spheres (48.2%) is lower than that of Fe₃O₄ spheres (70.7%) and higher than that of TiO₂@C hollow spheres (30.1%), implying that the irreversible capacity of Fe₃O₄@TiO₂@C Y-S spheres is largely derived from the outer TiO₂@C layer in the first cycle.

Figure 6 illustrates the galvanostatic discharge–charge voltage curves for the 1st, 2nd, 10th, 30th, 50th, and 100th cycles of Fe₃O₄@TiO₂@C Y-S spheres, Fe₃O₄ spheres, and TiO₂@C hollow spheres at 200 mA/g in a voltage range from 3.0 to 0.01 V. As shown in Fig. 6a, the voltage plateaus of Fe₃O₄@TiO₂@C Y-S spheres at about 1.75 V and 2.0 V are attributed to the insertion–extraction of lithium ions in the anatase TiO₂ layer with good crystallinity [20], while the voltage plateaus at about 0.75 V and 1.5 V correspond to

the redox reactions between Fe₃O₄ and Fe [12, 14–17, 19]. Notably, the formation of SEI films occurs in a voltage range below 0.75 V [19, 20].

The galvanostatic discharge–charge voltage profiles of pure Fe₃O₄ spheres are shown in Fig. 6b for comparison. It is evident that the same voltage plateaus at approximately 0.75 V and 1.5 V correspond to the redox reactions between Fe₃O₄ and Fe. Besides, the capacity fading is fast in the first five cycles, and then, it slows from the 6th cycle to the 10th cycle. The gradual increase in the space between the discharge–charge voltage plateaus suggests that the cell polarization caused by the high resistance, low ionic transport, and low electronic conductivity increases sharply with an increase in cycles during the first 10 cycles. Such poor electrochemical properties are mainly ascribed to the pulverization of active material and the crack of electrode caused by the severe volume expansion of bare Fe₃O₄ spheres. The pulverized Fe₃O₄ can lead to a loose connection between the particles and the current collector [20]. Then, the crack of electrode results in the rupture of SEI films, which forces the new electrode surface to be exposed to the electrolyte, and unstable SEI layers are then repeatedly formed and more electrolyte is consumed [12, 16]. Following this, the capacities and voltage plateaus tend to become stable.

The discharge–charge voltage profiles of TiO₂@C hollow spheres are shown in Fig. 6c, which indicates that the plateaus at about 1.75 V and 2.0 V are ascribed to the redox process of anatase phase TiO₂ crystals [20], and no other voltage plateaus are observed. In summary, the stable capacities and voltage plateaus indicate that the TiO₂@C layer has good electrochemical properties for application in LIBs. Therefore, coating the TiO₂@C layer is a good way for improving the cycling stability of the inner Fe₃O₄ spheres.

Figure 7a presents the rate capability of Fe₃O₄@TiO₂@C Y-S spheres at various current densities for 20 cycles. At a low current density of 50 mA/g, the first discharge capacity

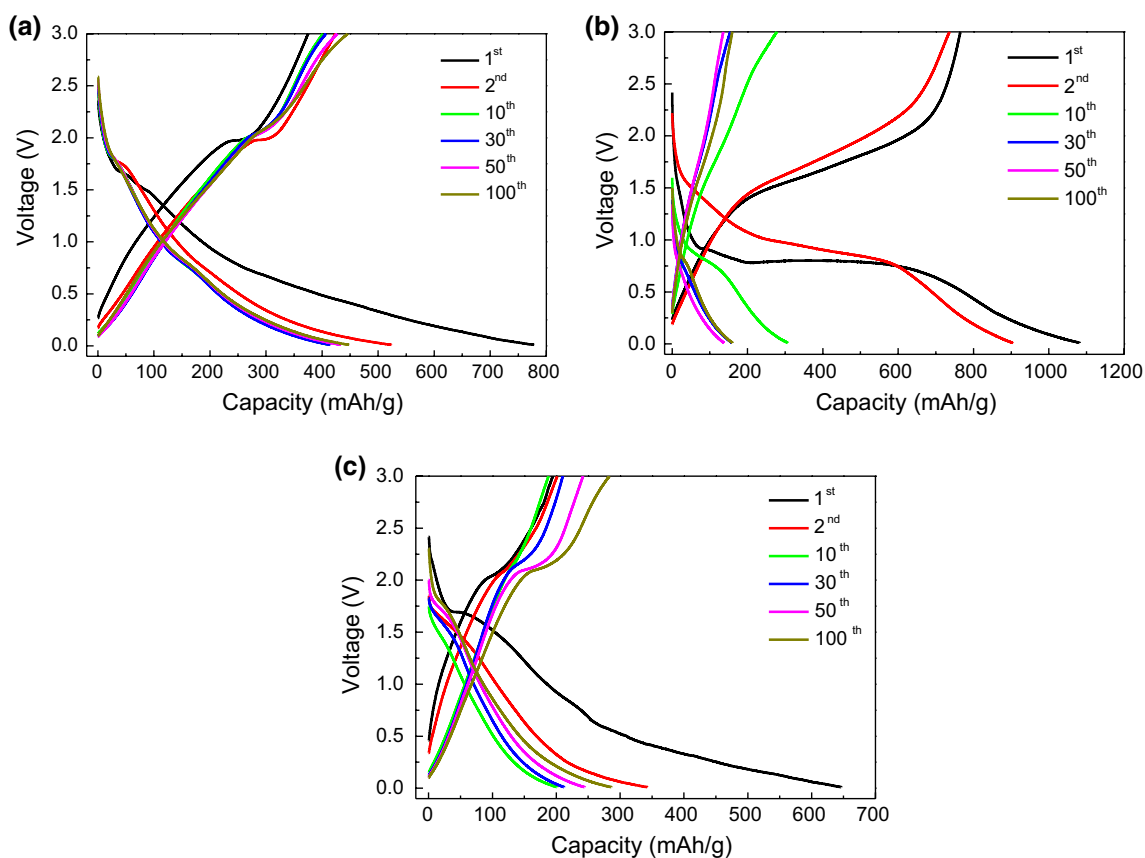


Fig. 6 Discharge–charge voltage profiles of **a** $\text{Fe}_3\text{O}_4@\text{TiO}_2@\text{C}$ Y–S spheres, **b** Fe_3O_4 spheres, and **c** $\text{TiO}_2@\text{C}$ hollow spheres at different cycles

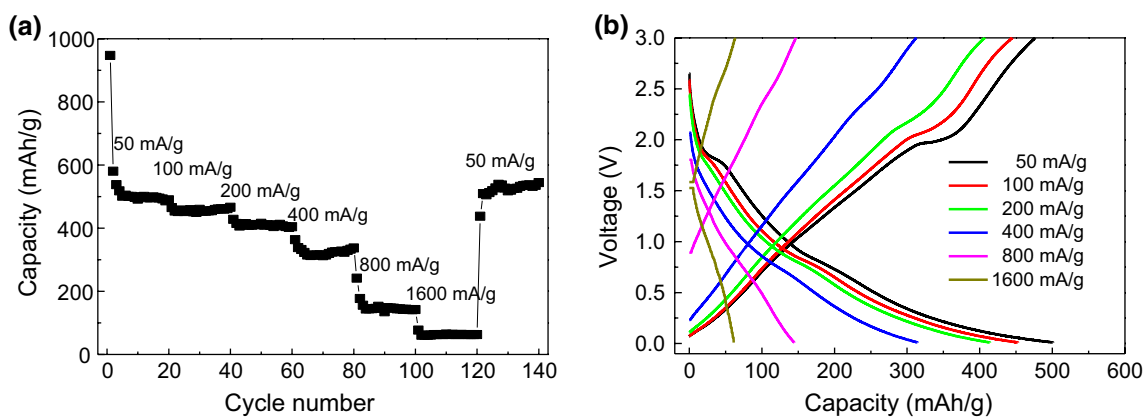


Fig. 7 **a** Rate performance and **b** discharge–charge voltage profiles of $\text{Fe}_3\text{O}_4@\text{TiO}_2@\text{C}$ Y–S spheres at various current densities

of $\text{Fe}_3\text{O}_4@\text{TiO}_2@\text{C}$ Y–S spheres is 950 mAh/g, and then, the capacities are stabilized at about 500 mAh/g in subsequent cycles. In addition, when the constant current densities are switched to 100 mA/g, 200 mA/g, 400 mA/g, 800 mA/g, and 1600 mA/g, the discharge capacities of $\text{Fe}_3\text{O}_4@\text{TiO}_2@\text{C}$ Y–S spheres remain at about 460 mAh/g, 410 mAh/g, 320 mAh/g, 150 mAh/g, and 62 mAh/g, respectively. When

the current density returns to 50 mA/g, the reversible capacities of $\text{Fe}_3\text{O}_4@\text{TiO}_2@\text{C}$ Y–S spheres still reach more than 500 mAh/g, indicating the excellent cycle stability and good reversibility.

Figure 7b shows the discharge–charge voltage profiles of $\text{Fe}_3\text{O}_4@\text{TiO}_2@\text{C}$ Y–S spheres at various current densities. It is evident that at low current densities (50–400 mA/g),

the fading of electrochemical reversible capacities, and the space of discharge–charge voltage plateaus increase slowly with the increasing current density. However, at high current densities (400–1600 mA/g), the fading of electrochemical reversible capacities, and the space of discharge–charge voltage plateaus increase sharply with the increasing current density. This can be attributed to three factors: (1) The middle layer TiO_2 is a kind of semiconductor material that affects the charge transfer and lithium ions diffusion in the interior Fe_3O_4 spheres; (2) the lower carbon content results in the low electron transfer and poor lithium ions diffusion; and (3) the accumulation or depletion of lithium ions on the electrode causes the concentration polarization of batteries due to slow diffusion at high current densities.

CV curves of bare Fe_3O_4 spheres and $\text{Fe}_3\text{O}_4@/\text{TiO}_2@/\text{C}$ Y–S spheres were measured at a lower scan rate of 0.10 mV/s in a potential range from 3.0 to 0.01 V (Fig. 8a, b). From Fig. 8a, in the first cycle, an obvious larger reduction current in the region of below 0.75 V should be mainly ascribed to the formation of SEI films and the reduction process of Fe_3O_4 , while the oxidation peak at 1.68 V can be attributed to the oxidation process from Fe to Fe_3O_4 [12, 16].

The related electrochemical reaction process is presented in Eqs. (1)–(3). Subsequently, the reduction peaks firstly shift to about 1.3 V and then shift to the lower potential, while the oxidation peaks constantly shift to the higher potential. The gradually decreased peak area and the increased peak space indicate the continuously increased rupture and volume expansion of Fe_3O_4 spheres, and the electrode polarization, resulting in a poor cycling stability and low reversible capacity [10–14]. This is well consistent with the galvanostatic discharge–charge tests of pure Fe_3O_4 spheres. From Fig. 8b, the electrochemical performance of $\text{Fe}_3\text{O}_4@/\text{TiO}_2@/\text{C}$ Y–S spheres obviously exceeds that of bare Fe_3O_4 spheres under the same test conditions. In the first cycle, a large and irreversible reduction current below 1.0 V corresponds to the formation of SEI films and the irreversible insertion of lithium ions in TiO_2 and Fe_3O_4 crystals [12, 14–16, 20]. A pair of symmetrical redox CV peaks situated at 2.0 V and 1.75 V are attributed to the redox potential of TiO_2 [20], while the redox CV peaks at 1.2 V and 0.75 V correspond to the redox potential of Fe_3O_4 [12, 14–16, 20].

The subsequent CV curves of $\text{Fe}_3\text{O}_4@/\text{TiO}_2@/\text{C}$ Y–S spheres were further measured to investigate the

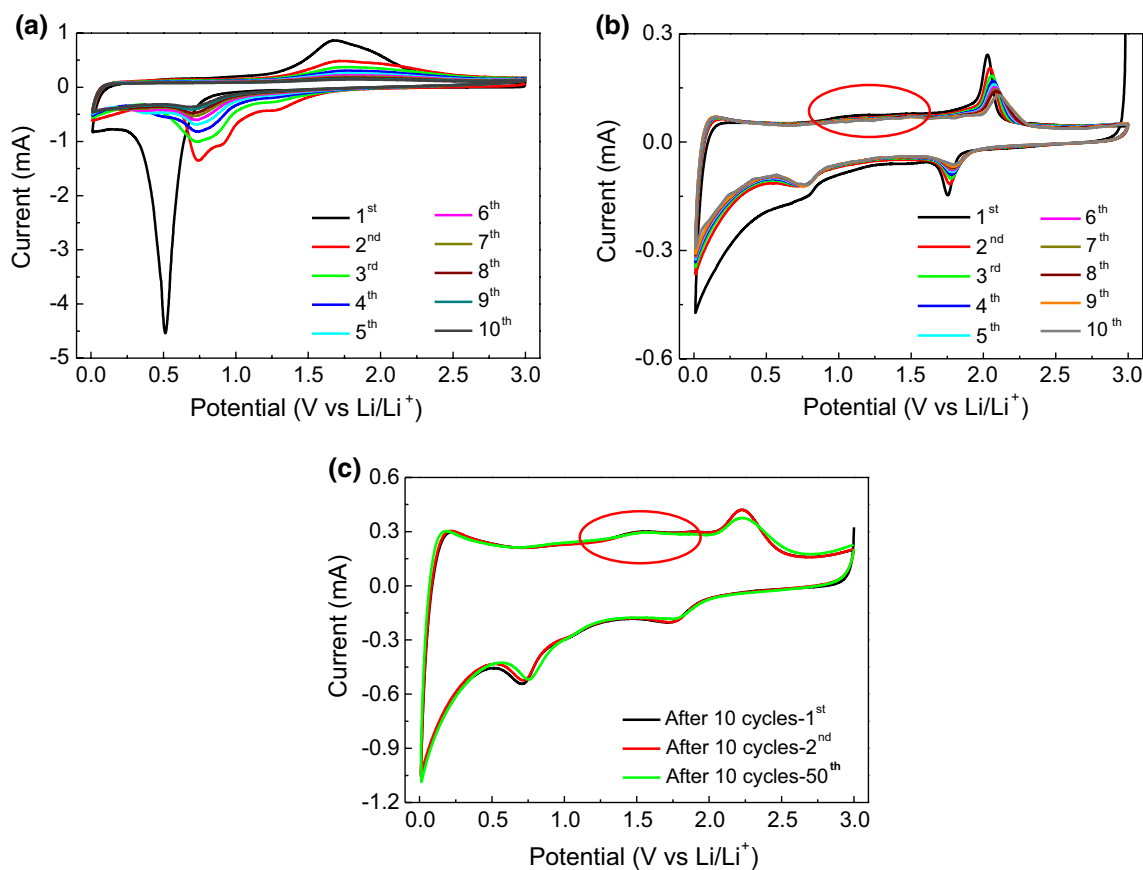
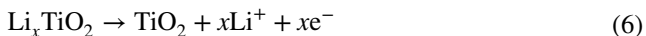
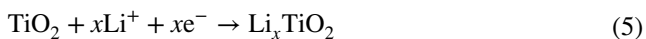
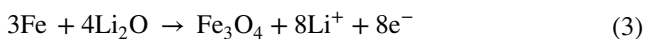
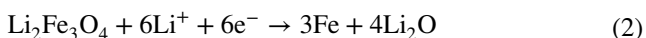
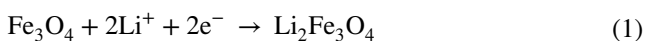


Fig. 8 First ten CV curves of **a** Fe_3O_4 spheres and **b** $\text{Fe}_3\text{O}_4@/\text{TiO}_2@/\text{C}$ Y–S spheres at a scan rate of 0.10 mV/s and **c** subsequent fifty times CV curves of $\text{Fe}_3\text{O}_4@/\text{TiO}_2@/\text{C}$ Y–S spheres at 0.50 mV/s in a potential range from 3.0 to 0.01 V versus Li/Li^+

electrochemical kinetics at a high scan rate of 0.50 mV/s (Fig. 8c). Compared with the tested CV curves at 0.10 mV/s, the redox peaks potential of TiO₂ shifts to 2.25 V and 1.75 V, while the anodic peak of Fe₃O₄ at 1.2 V (marked using one red circle in Fig. 8b) also shifts to 1.5 V (marked using another red circle in Fig. 8c). The wider space between the redox peaks indicates the increasing electrode polarization at a higher scan rate, which is in good agreement with the rate performance tests. In addition, there are no obvious changes in the shifts of peak areas and positions in the subsequent 50 cycles, indicating that the Fe₃O₄@TiO₂@C Y–S spheres possess a good cycling stability as LIBs' anodes. The results match well with the above galvanostatic discharge–charge cycle tests. The electrode reactions are described as follows:



Conclusions

The Stöber method was employed to successfully synthesize Fe₃O₄@TiO₂@C yolk–shell (Y–S) spheres for LIB anodes. The TiO₂@C shell and void space effectively alleviate the severe volume expansion of Fe₃O₄ spheres and restrict the rupture of electrodes, which thus improves the electrochemical performance throughout the cycles. At a constant current density of 200 mA/g, the Fe₃O₄@TiO₂@C Y–S spheres can release a high reversible capacity of approximately 450 mAh/g after 100 cycles, which is far higher than that of bare Fe₃O₄ spheres (160.2 mAh/g) and TiO₂@C hollow spheres (286.5 mAh/g). These results also demonstrate that the design of the Y–S structure can be applied in developing new type electrode materials for LIBs.

Acknowledgements This study was supported by the Tianjin Committee of Science and Technology (No. 14JCZDJC32400) and Tianjin Science and Technology Innovation Platform Program (No. 14TXGCCX00017).

References

- Meng YS, Wang GR, Xiao MJ et al (2017) Ionic liquid-derived Co₃O₄/carbon nano-onions composite and its enhanced performance as anode for lithium-ion batteries. *J Mater Sci* 52(22):13192–13202
- Feng MY, Tian JH, Xie HM et al (2015) Nano-silicon/polyaniline composites with an enhanced reversible capacity as anode materials for lithium ion batteries. *J Solid State Electrochem* 19(6):1773–1782
- Béguin F, Presser V, Balducci A et al (2014) Carbons and electrolytes for advanced supercapacitors. *Adv Mater* 26(14):2219–2251
- Shi YH, Ma DQ, Wang WJ et al (2017) A supramolecular self-assembly hydrogel binder enables enhanced cycling of SnO₂-based anode for high-performance lithium-ion batteries. *J Mater Sci* 52(7):3545–3555
- Yin XM, Chen LB, Li CC et al (2011) Synthesis of mesoporous SnO₂ spheres via self-assembly and superior lithium storage properties. *Electrochim Acta* 56(5):2358–2363
- Ge DH, Geng HB, Wang JQ et al (2014) Porous nano-structured Co₃O₄ anode materials generated from coordination-driven self-assembled aggregates for advanced lithium ion batteries. *Nanoscale* 6(16):9689–9694
- Sun HT, Sun X, Hu T et al (2014) Graphene-wrapped mesoporous cobalt oxide hollow spheres anode for high-rate and long-life lithium ion batteries. *J Phys Chem C* 118(5):2263–2272
- Qiu KW, Yan HL, Zhang DY et al (2015) Hierarchical 3D Co₃O₄@MnO₂ core/shell nanoconch arrays on Ni foam for enhanced electrochemical performance. *J Solid State Electrochem* 19(2):391–401
- Wang Y, Han ZJ, Yu SF et al (2013) Core-leaf onion-like carbon/MnO₂ hybrid nano-urchins for rechargeable lithium-ion batteries. *Carbon* 64:230–236
- Pan QM, Liu J (2009) Facile fabrication of porous NiO films for lithium-ion batteries with high reversibility and rate capability. *J Solid State Electrochem* 13(10):1591–1597
- Wang C, Wang DL, Wang QM et al (2010) Fabrication and lithium storage performance of three-dimensional porous NiO as anode for lithium-ion battery. *J Power Sources* 195(21):7432–7437
- Fan XL, Shao J, Xiao XZ et al (2014) Carbon encapsulated 3D hierarchical Fe₃O₄ spheres as advanced anode materials with long cycle lifetimes for lithium-ion batteries. *J Mater Chem A* 2(35):14641–14648
- Li KY, Chen H, Shua FF et al (2014) Facile synthesis of iron-based compounds as high performance anode materials for Li-ion batteries. *RSC Adv* 4(69):36507–36512
- Zhang XL, Hu ZB, Xiao XL et al (2015) Fe₃O₄@porous carbon hybrid as the anode material for a lithium-ion battery: Performance optimization by composition and microstructure tailoring. *New J Chem* 39(5):3435–3443
- Gu SZ, Liu YP, Zhang GH et al (2014) Fe₃O₄/carbon composites obtained by electrospinning as an anode material with high rate capability for lithium ion batteries. *RSC Adv* 4:41179–41184
- Gan YP, Gu HQ, Xiao H et al (2014) Mesoporous Fe₃O₄@C submicrospheres evolved by a novel self-corrosion mechanism for high-performance lithium-ion batteries. *New J Chem* 38(6):2428–2434
- Liang CL, Huang SC, Zhao WX et al (2015) Polyhedral Fe₃O₄ nanoparticles for lithium ion storage. *New J Chem* 39(4):2651–2656
- Lin YM, Abel PR, Heller A et al (2011) α -Fe₂O₃ nanorods as anode material for lithium ion batteries. *J Phys Chem Lett* 2(22):2885–2891

19. Geng HB, Zhou Q, Zheng JW et al (2014) Preparation of porous and hollow $\text{Fe}_3\text{O}_4@\text{C}$ spheres as an efficient anode material for a high-performance Li-ion battery. *RSC Adv* 4(13):6430–6434
20. Zhang X, Chen HX, Xie YP et al (2014) Ultralong life lithium-ion battery anode with superior high-rate capability and excellent cyclic stability from mesoporous $\text{Fe}_2\text{O}_3@\text{TiO}_2$ core-shell nanorods. *J Mater Chem A* 2(11):3912–3918
21. Zhao Y, Feng ZX, Xu ZJ (2015) Yolk-shell $\text{Fe}_2\text{O}_3@\text{C}$ composites anchored on MWNTs with enhanced lithium and sodium storage. *Nanoscale* 7(21):9520–9525
22. Wang BX, Wang ZQ, Cui YJ et al (2015) $\text{Cr}_2\text{O}_3@\text{TiO}_2$ yolk/shell octahedrons derived from a metal-organic framework for high-performance lithium-ion batteries. *Microporous Mesoporous Mater* 203:86–90
23. Wang JX, Li W, Wang F et al (2014) Controllable synthesis of $\text{SnO}_2@\text{C}$ yolk-shell nanospheres as a high-performance anode material for lithium ion batteries. *Nanoscale* 6(6):3217–3222
24. Cai ZY, Xu L, Yan MY et al (2015) Manganese oxide/carbon yolk-shell nanorod anodes for high capacity lithium batteries. *Nano Lett* 15:738–744
25. Liao WM, Tian JH, Shan ZQ et al (2018) Double-shelled $\text{Co}_3\text{O}_4@\text{TiO}_2@\text{C}$ yolk-shell spheres as anode material for enhanced cycling stability of lithium ion batteries. *J Alloy Compd* 739:746–754
26. Li W, Deng YH, Wu ZX et al (2011) Hydrothermal etching assisted crystallization: a facile route to functional yolk-shell titanate microspheres with ultrathin nanosheets-assembled double shells. *J Am Chem Soc* 133(40):15830–15833
27. Wang J, Zhao L, Lin VSY et al (2009) Formation of various TiO_2 nanostructures from electrochemically anodized titanium. *J Mater Chem* 19(22):3682–3687
28. Pradhan GK, Padhi DK, Parida KM (2013) Fabrication of $\alpha\text{-Fe}_2\text{O}_3$ nanorod/RGO composite: a novel hybrid photocatalyst for phenol degradation. *ACS Appl Mater Interfaces* 5(18):9101–9110
29. Akhavan O (2010) The effect of heat treatment on formation of graphene thin films from graphene oxide nanosheets. *Carbon* 48(2):509–519
30. Meng JK, Cao Y, Suo Y et al (2015) Facile fabrication of 3D $\text{SiO}_2@\text{graphene}$ aerogel composites as anode material for lithium ion batteries. *Electrochim Acta* 176:1001–1009
31. Liu SZ, Zhu KL, Tian JH et al (2015) Submicron-sized mesoporous anatase TiO_2 beads with trapped SnO_2 for long-term, high-rate lithium storage. *J Alloy Compd* 639:60–67



Jianhua Tian is a professor in Tianjin University. Her current interests concentrate on the development of novel electrode materials for advanced lithium ion batteries, dye-sensitized solar cells and supercapacitor.